PAPER • OPEN ACCESS

Fibre-optic measurement of strain and shape on a helicopter rotor blade during a ground run: 1. Measurement of strain

To cite this article: Stephen W James *et al* 2022 *Smart Mater. Struct.* **31** 075014

View the article online for updates and enhancements.

Fibre-optic measurement of strain and shape on a helicopter rotor blade during a ground run: 1. Measurement of strain

Stephen W James[1,*] , Thomas Kissinger[1,5] , Simone Weber[4,6], Kevin Mullaney[1], Edmond Chehura[1], Huseyin H Pekmezci[1,7], James H Barrington[1], Stephen E Staines[1], Thomas O H Charrett[1] , Nicholas J Lawson[2,8], Mudassir Lone[3,9], Richard Atack[4] and Ralph P Tatam[1]

[1] Engineering Photonics, Cranfield University, Bedfordshire MK43 0AL, United Kingdom
[2] National Flying Laboratory Centre, Cranfield University, Bedfordshire MK43 0AL, United Kingdom
[3] Centre for Aeronautics, Cranfield University, Bedfordshire MK43 0AL, United Kingdom
[4] Airbus Helicopters UK Ltd, Kidlington Oxfordshire OX5 1QZ, United Kingdom

E-mail: s.w.james@cranfield.ac.uk

Abstract
Optical fibre strain and shape measurement sensors were deployed on a 5-m long rotor blade during a full-speed (rotation rate 6.6 Hz) helicopter ground run, with real-time data wirelessly streamed from rotor hub-mounted sensor interrogators. In Part 1 of a 2-part paper series, the strain sensing capabilities of the two optical fibre-based sensing techniques, optical fibre Bragg grating (FBG) and fibre segment interferometry (FSI), are compared, while Part 2 (Kissinger *et al* 2022 *Smart Mater. Struct.* accepted) specifically investigates the blade shape measurement based on the FSI approach. In part 1, the rotor hub-mounted instrumentation is described, and data on the dynamics of the blade obtained from a sequence of controlled pilot inputs are analysed both in the time and spectral domains. It is shown that this can provide insights into the aeroelastic properties of the blade. Noise standard deviations of 0.2 nϵ/$\sqrt{\text{Hz}}$ and 30 nϵ/$\sqrt{\text{Hz}}$ for the FSI and FBG-based sensing approaches, respectively, were observed over a strain range of 3500 $\mu\varepsilon$.

[5] Now: Institute of Process Measurement and Sensor Technology, Technical University of Ilmenau, PF 100565, 98694 Ilmenau, Germany.
[6] Now: Airbus Helicopters Deutschland GmbH, Industriestrasse 4, 86609 Donauwöprth, Germany.
[7] Now: Arm-ECS Research Centre and Centre for Internet of Things (IoT) and Pervasive Systems, University of Southampton, Southampton SO17 1BJ, United Kingdom.
[8] Now: School of Aerospace, Mechanical and Mechatronic Engineering, The University of Sydney, NSW 2006, Australia.
[9] Now: Lilium GMBH, Munich, Germany.
[*] Author to whom any correspondence should be addressed.

(Some figures may appear in colour only in the online journal)

1. Introduction

The potential for the use of optical fibre sensors (OFSs) for the measurement of strain on aircraft structures has been well-documented [1]. OFS offer several advantages over conventional sensors, including their flexibility, low weight, electromagnetic immunity and small dimensions (diameter of order 0.2 mm), and the absence of a requirement for electrical connection to the sensor elements. These features can allow their use as surface mounted sensors on aerodynamic surfaces, as has been shown for fixed wing applications [2, 3]. In addition, optical fibres can be embedded within fibre reinforced composite structures and components during fabrication [4].

Rotor blades are considered to be one of the most safety critical systems of a helicopter, being susceptible to fatigue, impact damage and absorption of moisture, with the resulting structural degradation leading to reduced performance or potentially causing catastrophic failure [5]. Currently, the condition of the main rotor blades of a helicopter is assessed mainly during maintenance processes, via routine visual inspection and tap testing [6]. During track and balance procedures, information can be gained via measurements of the 1/rev vibration signal coupled from the rotor to fuselage-mounted accelerometers, and by blade position monitoring [7, 8]. While there is interest in the deployment of sensors on the blade [5], currently available sensing technologies are not suited to the direct measurement of main rotor characteristics in-flight. Accelerometers, along with the associated wiring loom, are typically bulky and their mounting in the rotating frame could interfere with the aerodynamics and structural dynamics of the blade. In addition the accelerometer measurements comprise a superposition of the desired vibration measurements with the signals corresponding to the centrifugal acceleration of the blade and overall helicopter movement. Electrical strain gauges have been employed in-flight to monitor the structural deformation of rotor blades [9–11]. However, in addition to the deleterious influence of the wiring on the aerodynamics and the dynamic behaviour of the blade, long installation times, and their sensitivity to temperature and water ingress can also limit their utility. It has been noted that strain gauges often fail during testing and that the quality of the data can be compromised by noise on the electrical slip rings that are often used to transfer the data from the rotating frame to the fixed frame [12].

To-date, aerospace applications of OFS have predominantly concerned their use on fixed-wing aircraft [2, 3, 13–17], with examples of flight tests with OFSs bonded to the wings of a twin turboprop aircraft, Jetstream 31 [3], and to the wings of an aerobatic single propeller aircraft, Scottish Aviation Bulldog [2], measuring strain during extreme manoeuvres including banked turns [3], stall turns, barrels rolls, loops and spins [2]. The use of OFS on rotorcraft has been been less widely reported. In laboratory settings, OFS have

been used to detect damage on a rotor blade [6] and have been deployed in a ground vibration test of a bearingless main rotor (BMR) blade to characterise the blade's structural dynamics [18, 19]. OFS have been deployed on a scaled helicopter rotor operated in a wind tunnel to estimate its tip displacement by using a shape reconstruction algorithm [20], and have been integrated into the root of a BMR blade [21], where the measured strain was used in the calculation of the useful remaining life of the blade. Recently, fibre optic strain sensors were used for in-flight measurements on a T-22 helicopter [22]. Six sensors multiplexed in a single length of optical fibre were connected to a battery-powered interrogator located at the top of the rotor mast. To measure the strain in the lead-lag direction, sensors were mounted either side of the neutral axes in the chord-wise direction, while monitoring the through-thickness (flapping) strain was achieved by mounting sensors near the leading and trailing edges, oriented along the span of the blade. Two OFS were oriented at $+45°$ and $-45°$ to the span-wise axis to provide information on the torsional modes. It was reported that lead-lag, flap and torsion deformations could be detected, and it was suggested that signals related to rigid body motion could be distinguished from the blade's aeroelastic behaviour. A recent publication proposed a method for the structural health monitoring of helicopter blades exploiting the difference of strain or shape signals between rotor blades [5], for which optical fibre based measurement approaches would be ideal.

This 2-part paper presents research undertaken as part of the BladeSense (*Measurement of Dynamic Rotor Blade Deformation*) project [23], which aimed to investigate the use of advanced optical fibre-based sensors on helicopter rotor blades to provide data to enhance the understanding of aerodynamic and aeroelastic phenomena, and with a view to exploring the feasibility for routine in-flight deployment, to facilitate rotor blade predictive maintenance. The ability of OFS technology to allow the analysis of the the vibration characteristics of a rotor blade in a stationary reference frame during a ground vibration test under laboratory conditions has been established previously by the authors [19]. In these papers, the use of the technology in the rotating frame is assessed during a series of helicopter ground runs, with OFS-instrumented rotor blades and the associated interrogation instrumentation mounted on a helicopter rotor hub. The project explored the use of OFS to monitor strain, which is the subject of Part 1, and to measure directly changes in the shape of the rotor blade, which will be detailed in Part 2 [24].

In this paper, Part 1, the deployment of two types of intrinsic OFS strain sensing technologies, fibre Bragg gratings (FBGs) and fibre segment interferometry (FSI), on a BMR blade of an Airbus Helicopters H135 helicopter during a full-speed ground run is described. Data were streamed wirelessly from rotor hub-mounted sensor interrogators to a ground station. The dynamics of the blade were monitored during a

sequence of controlled pilot inputs, providing insights into the aeroelastic properties of the blade and facilitating a comparison between the performances of the sensing systems.

2. Instrumentation

2.1. Sensing technologies: FBGs

The previously reported rotorcraft applications of OFS summarised in section 1 employed FBGs, which are in-fibre strain sensors of typical gauge length 5 mm. An FBG takes the form of a hologram formed in the core of the optical fibre that acts to reflect a narrow band of wavelengths (typically < 0.5 nm) back along the optical fibre when interrogated by a broadband optical source or widely tuneable laser. The reflection band is centred on the Bragg wavelength, which is related to the period of the grating and the effective refractive index of the propagating mode. Perturbations of the fibre that alter the period and/or refractive index result in a change in the reflected Bragg wavelength, the measurement of which forms the basis of operation of the sensing technology [25]. The change in the Bragg wavelength is directly proportional to the applied strain. FBG sensors are often deployed in a serial array within an optical fibre, with multiplexing achieved by fabricating each sensor with a distinct Bragg wavelength that can be uniquely resolved by the interrogator over the range of anticipated operating conditions. FBGs represent a relatively mature technology that is commercially available, with the flight-certified SmartScan Aero Mini interrogator deployed here allowing the simultaneous interrogation of sensors contained in four optical fibres, with each fibre containing up to 16 wavelength division multiplexed FBG sensors, at a data rate of 2.5 kHz, with quoted strain resolution of 1 $\mu\varepsilon$ [26].

2.2. Sensing technologies: FSI

FSI [27] is a new, optically and mechanically robust approach to the demodulation of the signals from an array of intrinsic interferometric strain sensors, which is capable of providing a strain resolution of sub n$\epsilon/\sqrt{\text{Hz}}$ at high data rates, up to 100 s of kHz. The approach, illustrated in figure 1, uses an optical system comprising a telecommunications distributed feedback (DFB) laser, a fibre optic circulator and a photo-diode to interrogate fibre segment interferometers formed between an array of in-fibre reflectors, exploiting the range resolved interferometry (RRI) signal processing technique [28].

In RRI, the sinusoidal modulation of the optical frequency of the output from the DFB laser, achieved by direct modulation of the injection current, imposes a range-proportional phase modulation on the interferometers formed between each in-fibre reflector and a reference reflector, typically the cleaved end face of the optical fibre. This generates a unique range-dependent carrier signal for each reflector that allows the phase measurement and multiplexing of the corresponding interferometer signals. Subtraction of the signals obtained from adjacent reflectors results in a measurement of the integrated strain signal between the two reflectors, i.e. over a fibre segment [27].
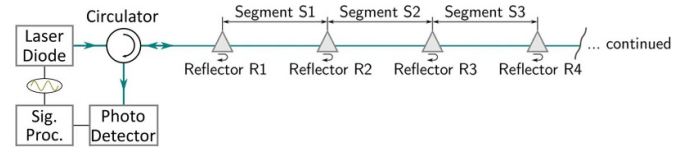

Figure 1. Typical FSI setup.

2.3. Sensor deployment

The rotor blades were instrumented with OFSs positioned along the leading edge. The sensor arrays were terminated at approximately 55% of the rotor length, which corresponds to the section of the leading edge that is routinely covered by a blade protection tape to avoid damage caused by minor impacts and erosion due to rain, sand, dirt, or other debris. All fibre optic sensors were covered by the blade protection tape to ensure safe operation during the ground runs and to simplify the certification process undertaken to obtain approval for ground testing.

Four FBG sensor arrays, each containing 10 wavelength-division-multiplexed FBGs, were fabricated in-house in hydrogen loaded SMF 28 optical fibre, with the sensors optimally distributed along a 2.1 m length of the fibre to ensure that the aeroelastic modes of interests could be captured with the number of sensors available. Arrays of FBGs were positioned 35 mm chordwise from the leading edge (equivalent to 12% of the mean aerodynamic chord of the blade) on the upper and lower surfaces of two rotor blades, with the final sensor in each array located at approximately 2.8 m from the centre of rotation. The sensors were bonded to the blade using cyanoacrylate adhesive. The locations of the sensors are illustrated in figure 2. The arrays were interrogated using a commercial FBG interrogator, SmartScan Aero Mini (SmartFibres, UK).

Arrays of 11 ultra short and low reflectively fibre Bragg gratings (LR-FBGs) were fabricated in-house in eight lengths of hydrogen loaded SMF 28, with adjacent LR-FBGs separated by 190 mm. The LR-FBGs were not interrogated in the spectral domain as FBG sensors typically are, but acted merely as the reflectors to form an array of low finesse Fabry–Perot cavities, the fibre segment interferometers. The reference was provided by the Fresnel reflection from the cleaved fibre end, located 95 mm from the final LR-FBG, which was protected from contamination and damage by encasing within a plastic tube. The interferometers were interrogated and demodulated using the RRI approach outlined in section 2.2. The LR-FBGs, each of length 250 μm and reflectivity 10 to 100 ppm, exhibited a broad reflection bandwidth, with FWHM 5 nm, which ensured that a reflection was achieved at the laser wavelength irrespective of the overall strain and/or temperature experienced by the LR-FBG. The spectral characteristics were similar to those presented in [29], and so are not presented here.

For the interferometric strain sensors discussed in this paper, the fibre of interest was one of a set of four optical fibres that were integrated within a flexible plastic rod that was designed to facilitate direct fibre optic shape sensing (DFOSS), which will be discussed in detail in Part 2 [24]. In Part 1 of this work—this paper—the strain signals from fibre string C,
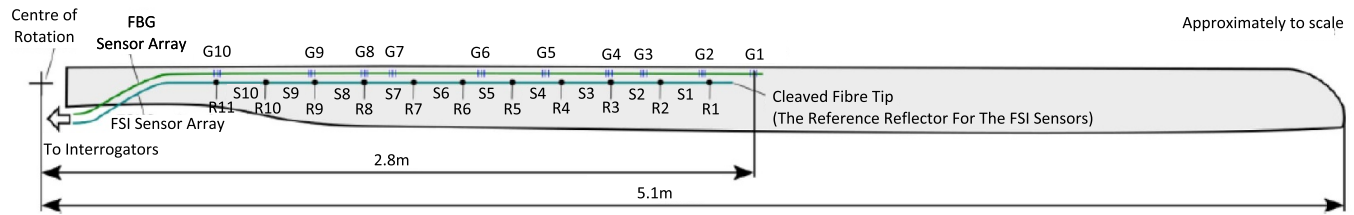
Figure 2. Diagram showing positions of the fibre sensors deployed on the lower surface of the rotor blade, with FBGs G1 to G10 and FSI sensing segments S1 to S10 shown. The black dots in the FSI sensor array represent the locations of the FSI reflectors, R1 to R11.

which was located close to the helicopter blade surface in the plastic rod assembly, was evaluated purely as an array of FSI strain sensors, while in Part 2 [24], strain signals from multiple fibre strings integrated within the plastic rod are used to perform DFOSS.

The fibres were bonded using cyanoacrylate into slots machined along the length of the rod, described in Part 2. The rod itself was attached to the blade using cyanoacrylate adhesive. The locations of the FSI sensor elements in the span wise direction along the blade are shown in figure 2, with reflectors, R1 to R11, and the corresponding segments, S1 to S10, formed between them, indicated. The DFOSS sensor rod was located approximately 15 mm from the leading edge, attached to the lower side of the blade. In this way the the surface disturbance was positioned ahead of the expected peak blade suction, reducing its influence on the aerodynamic performance of the blade. For the remainder of this paper, the FSI sensors and instrumentaion are referred to as FSI/DFOSS.

For redundancy, two blades were instrumented with the OFS, but only one blade was monitored during each ground run. To minimise potential issues with the balance of the 4-rotor blade assembly, the other two blades were prepared in the same way, but the optical fibres and sensing rods did not contain sensors.

2.4. Hub instrumentation assembly

Two customized hub support cap assemblies were constructed, one for the FBG sensing instrumentation, the other for FSI/DFOSS instrumentation. Each hub support cap assembly contained the appropriate sensor interrogator, a computational unit (in the form of a ruggedised miniature PC) and dedicated Wi-Fi card for data telemetry, an SSD drive that was used to store data locally as a backup and a Li-ion battery offering up to 6 h running time.

A schematic of the assembly is shown in figure 3. All optical fibres deployed on the blade were connected to the hub support cap assembly using Radial LuxCis® ARINC 801 connectors via bulkhead adapters.

Each hub support cap assembly also contained a power management unit (PMU) that controlled the LI-ion battery cells. The PMU was designed to allow the power to the instrument to be cut (through control signals sent over the Wi-Fi link) by the pilot in an emergency, and to be cut autonomously if the battery temperature rose above a predefined threshold or if Wi-Fi connection to the ground station was lost. Prior to the ground test, all components were tested rigorously under
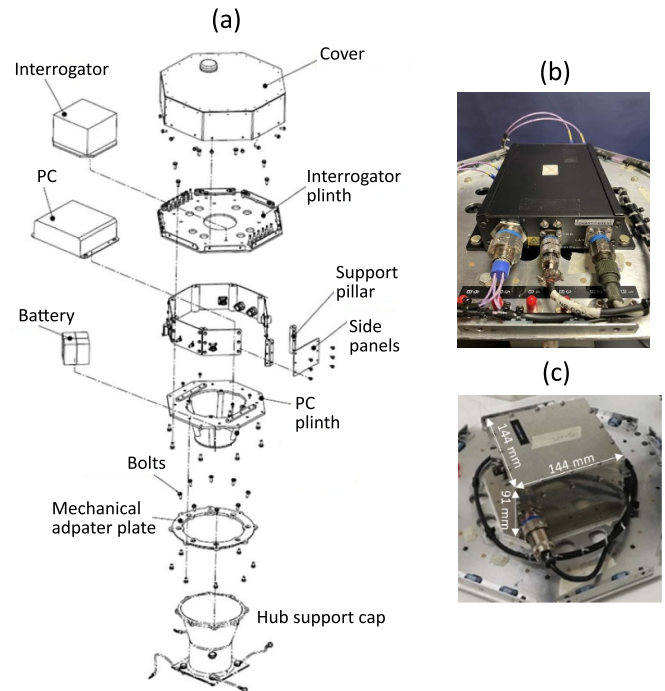

Figure 3. (a) Illustration of the layout of the hub support cap assemblies, (b) image of the Smartscan Aero Mini FBG sensor interrogator, (c) image of the FSI /DFOSS sensor interrogator. The width of the top cover of top cover plate was 360 mm, while the overall height of the assembly was 400 mm and the weight was approximately 11 kg.

vibration conditions analogous to that which would be experienced during the ground run, and the functionality of the units and Wi-Fi telemetry, when operated in the rotating frame at representative rotation rates, was assessed. In addition, the hub support caps were balanced by attachment of weights to the assembly, prior to installation on the helicopter. The FSI/DFOSS hub support cap assembly contained an in-house designed and constructed FSI/DFOSS interrogator for four input fibres, which allowed the real-time interrogation of 11 reflector signals, i.e. ten fibre segments, per fibre input. This instrument, shown in figure 3(c), comprises a DFB laser, fibre-optic components, photo detectors, an A–D converter, and a field-programmable gate array to provide the modulation signal to the laser drive current and to undertake processing of the phase of the returned signals from each interferometer. While the instrument is capable of resolving interferometric bandwidths up to 100 kHz, in this experiment, in order to lower

noise, a reduced interferometric bandwidth of 33 kHz was chosen. Furthermore, the interferometric data was decimated to a data rate of 3.2 kHz in order to lower the real-time data transfer load over the wireless link. Fibre optic patch cords connected the FSI/DFOSS interrogator to bulkhead adapters that were mounted in the hub support cap assembly.

The FBG hub support cap assembly housed a 4-channel SmartScan Aero mini interrogator [26] (shown in figure 3(b)), operating at a data rate of 2.5 kHz. The interrogator was selected due to its low profile, its performance specifications and its airworthiness certification standard, equivalent to MIL-STD 810G. The interrogator was connected to the bulkhead adapters mounted in the hub support cap assembly using patchcords terminated with Radial LuxCis® ARINC 801 connectors.

The helicopter was equipped with a range of other sensing technologies, including a health and usage monitoring system, Helitune's HT-VHM, incorporating a RT-TipTrak camera system to measure the blade tip deflection and a 6-axis sensor that monitored acceleration and rotor speed. An aspect of the project involved the demonstration of the ability to stream data to the HT-VHM from the ground station PC.

Figure 4(a) shows a hub support cap assembly mounted on the rotor mast. The optical fibre connections to the instrumentation via the bulkhead connectors can be seen. The route of the FSI/DFOSS sensing rod under the blade protection blade is also visible. The Airbus H135 helicopter, seen in figure 4(b) was fitted with large tanks that were filled with water to provide sufficient weight to prevent the helicopter taking off even when operated at full rotor speed.

3. Experimental conditions: ground runs

To assess the performances of the OFS technologies, ten ground runs of the helicopter were undertaken over 3 d, as detailed in table 1. The assessment of each sensing technology involved the installation of the relevant balanced hub support cap assembly onto the mast, shown in figure 4 and undertaking two short track and balance runs to adjust and verify the balance of the blades. A series of ground runs, GR1, GR2 and GR3 was then undertaken. The rotor was initially run up to its idling speed of 5 Hz, which was maintained for up to 2 min, before running up to full speed of 6.6 Hz.

Here the results from the 3rd ground runs (GR 3) with the FSI/DFOSS and FBG hub support caps installed will be presented, with the aim of providing data that is representative of the performance of the sensors.

3.1. Pilot inputs

When the rotor was operating at full speed, the pilot made discrete inputs to the collective and cyclic controls, with the set of inputs repeated three times during each ground run. The collective control changes the pitch angle of all the main rotor blades simultaneously, changing the lift uniformly across the rotor disk. In the collective manoeuvre, the collective was first stepped in the manner indicated in figure 5(a), which used
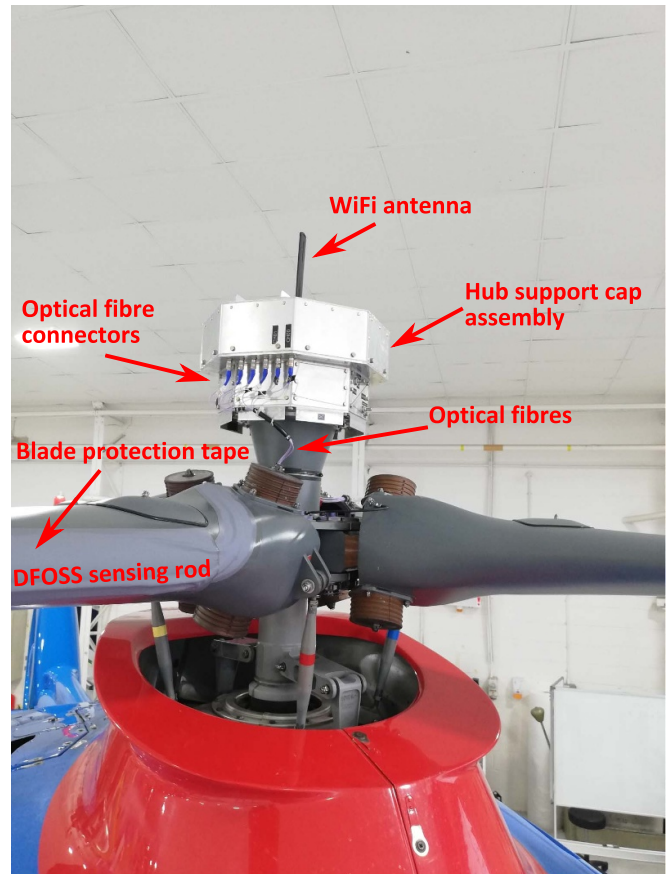
(a)

(b)

Figure 4. (a) Hub support cap assembly mounted on the rotor mast, (b) helicopter with hub support cap and instrumented blades during a ground run.

flight torque measurement as an indicator of the collective settings. The collective was also subject to two movements to 80% torque, figure 5(b)), termed a collective doublet.

The cyclic control changes the pitch angle of two opposing main rotor blades causing either a pitch attitude or roll response due to the resulting non-uniform lift distribution. It is used to introduce longitudinal or lateral movement. The cyclic control was subjected to a doublet cyclic lateral and doublet cyclic longitudinal. During the doublet cyclic lateral, the cyclic stick, originally in the neutral position, was moved to the right,

Table 1. Details of the test campaign.

FSI/DFOSS Hub Support Cap Installed		
Run	Length	Notes
T&B 1	8 min	Track and Balance
T&B 2	8 min	Track and Balance
GR 1	20 min	Ground run with pilot inputs to collective and cyclic controls
GR 2	20 min	Ground run with pilot inputs to collective and cyclic controls
GR 3	20 min	Ground run with pilot inputs to collective and cyclic controls
FBG Hub Support Cap Installed		
T&B 1	8 min	Track and Balance
T&B 2	8 min	Track and Balance
GR 1	20 min	Ground run with pilot inputs to collective and cyclic controls
GR 2	20 min	Ground run with pilot inputs to collective and cyclic controls
GR 3	20 min	Ground run with pilot inputs to collective and cyclic controls

Figure 6. FBG sensor data. (a) Wavelength shift exhibited by the sensors mounted on the lower surface f the blade, G1–G10. (b) Rotation rate determined from the data from G3. (c) and (d), detailed time series data for the FBGs during idle and full speed operation of the rotor, respectively.
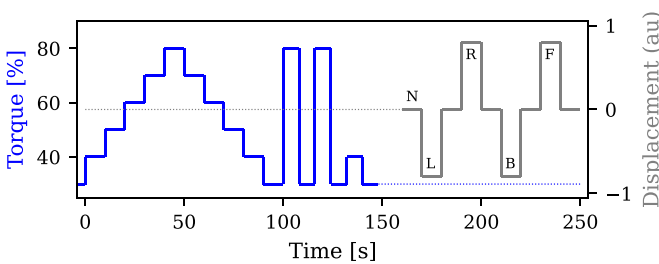

Figure 5. Planned pilot input pattern to the collective and cyclic controls; stepped collective (0–100 s), collective doublet (100–150 s), cyclic (160–250 s), N—neutral, L—left, R—right, B—backward, F—forward.

returned to the neutral position, before being moved to the left and finally returning to the neutral position. Similarly, during the doublet cyclic longitudinal, the cyclic stick was moved backwards from the neutral position, returned to the neutral position before moving forward and finally returning to the neutral position.

Results and discussion

4.1. Raw data

Figures 6 and 7 show the raw data obtained from the FBG and FSI sensors [30]. Figure 6(a) shows the measured changes in the wavelengths of each of the FBG sensors in the array bonded to the lower side of the blade. The step changes in wavelengths observed as the rotor transitions from stationary to idling are a result of a combination of the centrifugal forces and the change in shape of the blade as it rises from its initially drooped state. The further increase in wavelengths during the
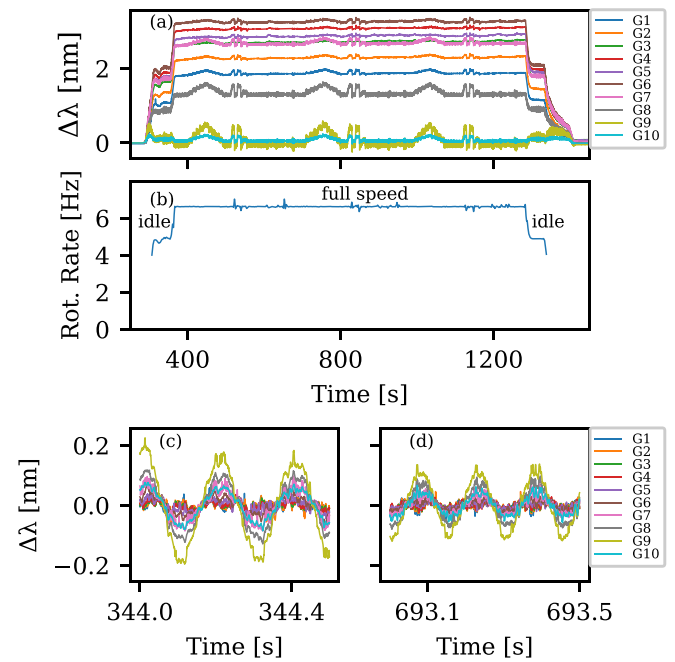
transition from idling to full speed operation are predominately a result of the additional centrifugal forces. The features in the time series observed during full speed operation correspond to the three repetitions of the pilot input sequence shown in figure 5. Analysis of the time series allows the determination of the helicopter rotation rate, shown in figure 6(b). This was calculated from the zero-crossings of the characteristic once per revolution signal, apparent in the 0.5 s duration slices of the time series shown in figures 6(c) and (d), which correspond to idle and full speed operation, respectively. The rotation rates in the idle condition and full speed conditions were 5 and 6.62 Hz, respectively, matching the measurements from the HMV system. Observation of data during idle and full speed operation (figures 6(c) and (d)) suggests the presence of a richer vibration frequency spectrum, which will be discussed in section 4.3.

In the case of FSI, figure 7(b) shows the phase changes measured for the interferometers formed between the each of the reflectors R1 to R11 and the reference reflection from the cleaved fibre end. As the FBG and FSI data were obtained during separate ground runs (because the interrogators were mounted in different hub support cap assemblies), the durations of idle and full speed operation sections of the runs differ, but the features of the data are similar. The data indicates that the interferometer with the longest length, corresponding to that between reflector R11, which was closest to the root of the blade, and the cleaved fibre end, exhibits the largest cumulative phase excursion. The amplitude of the phase excursion can be seen to reduce with decreasing interferometer length. The FSI data could also be analysed to allow the rotation rate to be determined, as shown in figure 7(b), with the measurements
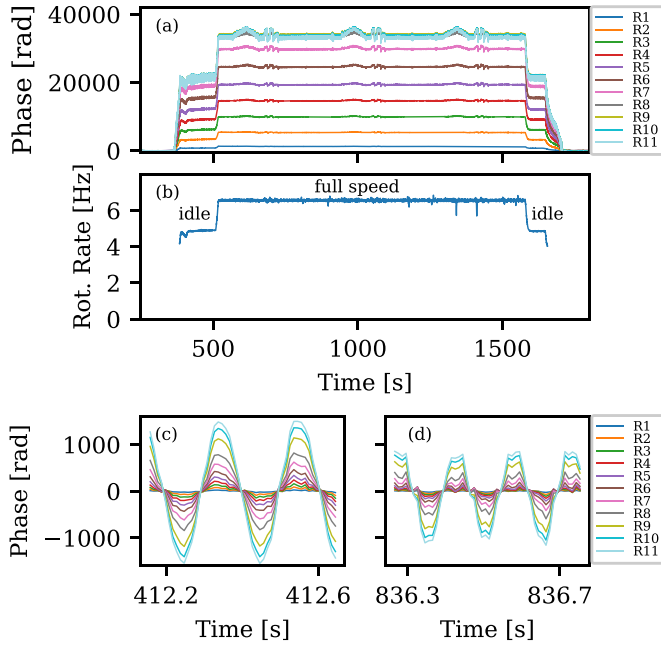
Figure 7. FSI sensor raw data. (a) Phase measurements from the interferometers formed between the reflectors (R1–R11, with R1 closest to the cleaved fibre end) and the reflection from the cleaved fibre end. (b) The rotation rate determined from the phase data. (c) and (d) detailed time series data for the interferometers during idle and full speed operation of the rotor, respectively.

matching that obtained from the FBG sensors. Comparison of the 0.5 s data slices at idle and full speed from the FBG (figure 6(c)) and FSI and (figure 7(c)) suggests that the FSI has significantly lower noise, which will be established in section 4.2.

4.2. Strain measurements

In the case of the FBG sensors, the strain, ε, is determined from the measured wavelength shift, $\Delta\lambda$, using equation (1)

$$\frac{\Delta\lambda}{\lambda} = (1 - p)\epsilon \tag{1}$$

where p is the strain optic coefficient of the fibre, typically of value 0.22 [31].

For FSI, the strain within the segments formed between adjacent reflectors is determined by subtracting the phases of the interferometers formed between each of the reflectors and the cleaved fibre end. The strain is then related to the phase change, $\Delta\theta$, in the fibre segment interferometer via equation (2) [32]

$$\epsilon = \frac{\Delta\theta \cdot \lambda}{2l_{\mathrm{g}} \cdot 2\pi \cdot n_{\mathrm{eff}} \cdot k}. \tag{2}$$

Here λ is the vacuum wavelength of the laser light and k is the strain sensitivity factor of the fibre. We take k to be 0.795 for SMF-28 type fibre [33] and the effective refractive index of the fibre core as $n_{\mathrm{eff}} = 1.45$. An additional factor of two in the denominator is included because the light passes through the sensor gauge length, l_{g}, twice. It should be noted that, since

both the FBG and FSI measurements are dependent on the same glass properties of the optical fibre, for homogeneous structural strains no principle differences in the readings are expected if the strain transfer to the sensing fibres is equally well established.

Figure 8 shows the time-series of the strain measurements obtained from the two systems during comparable ground runs and for approximately co-located sensor positions, where a sequence of controlled pilot inputs, shown in figure 5, were applied with the aim of exciting the blade dynamics. It is important to note that the data presented represents two separate ground runs, as the FBG and FSI/DFOSS interrogators were mounted in two separate hub support caps, which were swapped between runs. However, it can be seen that the overall strain magnitudes achieved with both systems are comparable, as can be seen from the measured strain distributions (averaged over 20 s) during idle and full speed operation sections of the ground run, plotted in figure 9. The small, typically <10%, differences are attributed to the different positions of the sensors, and it is suggested that differences are to be expected when comparing highly localized FBG sensors, with gauge lengths of 4 mm, with FSI sensors with gauge lengths of 190 mm.

In figure 9, to reflect the fact that the FSI measurements are integrated over the length of each segment, the FSI-measured strain is plotted as being located at the centre of each segment. The maximum rate of change of strain is observed between 1 and 1.5 m along the blade, corresponding to the location where the pitch control cuff merges with the main structure of the blade [19]. The maximum strain, which is predominantly a result of centrifugal tensile loading, is experienced around one third of the rotor length, which then continuously decreases towards the blade tip. The sensor elements closest to the centre of rotation (FBG sensors G1 and G2, and FSI segments S1, S2 and S3) are mounted on the cuff, a section of the blade that is designed not to flex and not to carry the centrifugal force [34], and thus experience significantly smaller loads, and, in the case of G1, S1 and S2, even compressive loading. This is a result of the change in the rotor blade state from non-rotating to rotating, since the baseline measurements were recorded when the blade was in the drooping, non-rotating condition. The generally very good mutual agreement between the FSI and FBG sensor measurements exhibited in figure 9, where FBGs measure local strain over their 4 mm gauge lengths while the FSI sensors measure averaged strain values over a 190 mm long segment, as well as the continuous nature of the measured strain function without obvious outlying data points, provides a strong indication that strain transfer is likely to be well-established for both types of sensor.

In figure 8(b), the time series for segment S10 reveals a discontinuity at ≈900 s, which leads to a persistent error in the strain measurement for this segment. As discussed previously, the real-time acquisition was performed at a reduced interferometric bandwidth of 33 kHz. Unfortunately, in this singular case, the chosen bandwidth proved too low to resolve the rapid fringe rates that occurred, as segment S10 was located furthest away from the interferometric reference, the fibre tip, and therefore exhibited the highest interferometric fringe rates of the array of interfeometers. In future experiments, the
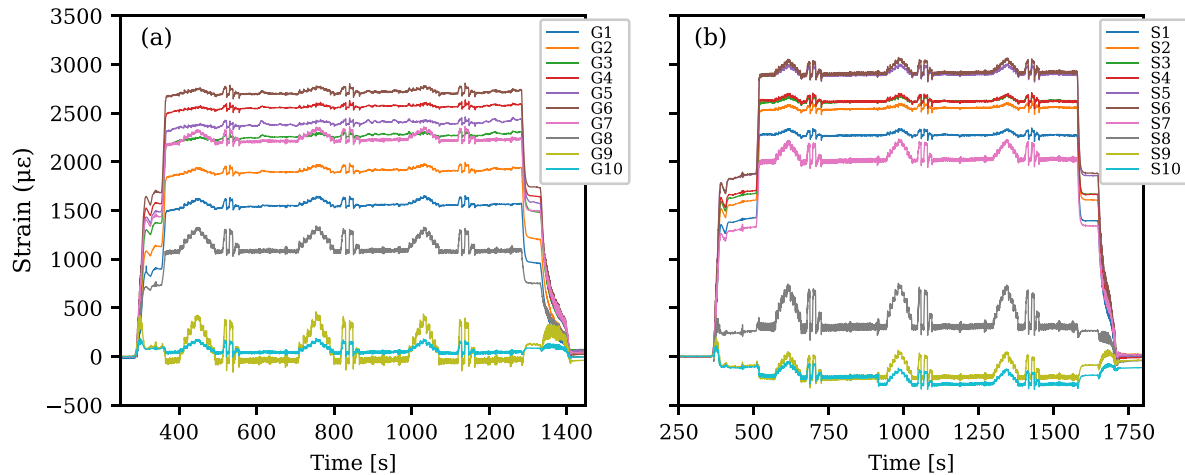
Figure 8. Strain data, time-averaged to an equivalent of a 5 Hz data rate, obtained during two separate ground runs for all of the sensors in (a) the array of FBGs attached to the lower surface of the blade (G1–G10, FBG sensors) and (b) the array of FSI sensors attached the lower surface of the blade (S1–S10, fibre segment interferometers).
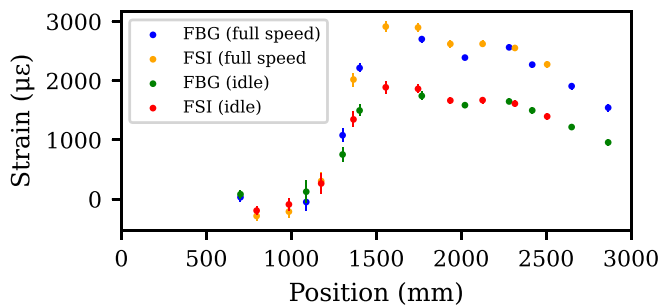

Figure 9. Distribution of measured strain along the blade under idle and full speed operation. The strain from the FSI sensors is plotted at the centre of each FSI segment.

safety margin in the interferometric bandwidth setting should be increased, to prevent such issues occurring.

It should be noted that the measurements presented here are not corrected for the influence of temperature. A computational fluid dynamics study of the aerofoil section (not presented) suggested that under the test conditions, the local air temperature at the location of the sensors closest to the centre of rotation, would be raised by $<5°$, with a corresponding thermal apparent strain of $<50~\mu\epsilon$, while at the location of the sensors furthest from the centre of rotation the change would be $<10°$ with a corresponding thermal apparent strain of $<100~\mu\epsilon$. The time series shown in figure 8 do show positive changes in strain between the starts and ends of the idling and full speed sections of the trial, which may be caused by an increase in the temperature of the blade. There are a number of approaches to the discrimination between temperature and strain for FBG sensors [35]. In this case, however, as the main focus of the analysis is on the blade dynamics, it is less critical to compensate for temperature in these measurements.

To provide a direct comparison of the signals obtained by the two fibre optic sensing approaches, figure 10 shows plots of comparable 1 s duration sections of the data time series (at full data rate), encompassing approximately six rotations of
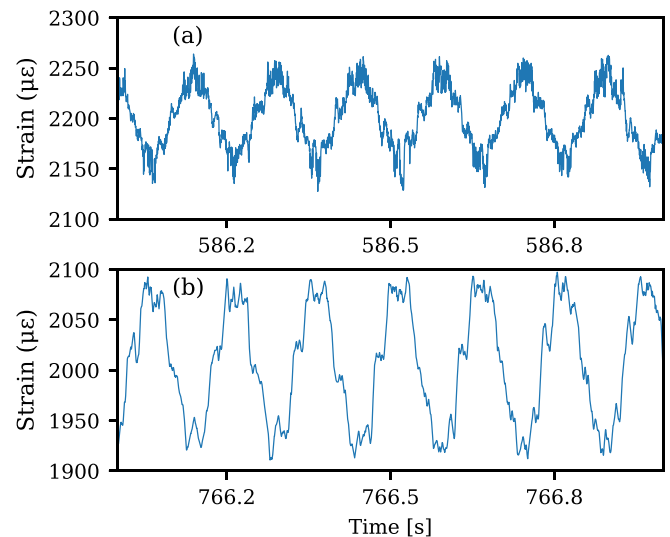

Figure 10. Strain data at full data rate, extracted from the time series shown in figure 8, representing six rotations of the rotor at full speed. (a) FBG sensor G7 attached to the lower surface of the blade 1.4 m from the centre of rotation and (b) FSI sensor S7 attached to the lower surface of the blade, with its centre located 1.4 m from the centre of rotation.

the rotor at full speed, for FBG G7 and FSI segment S7. These sensors were approximately co-located. The higher quality of the measurements provided by the FSI technique, compared to that provided by the FBG interrogation approach used here, is clearly visible when comparing figures 10(a) and (b).

The FBG and FSI sensor responses to the three repeated sequences of pilot control inputs are shown in more detail in figure 11. For the 2nd repeat of the pilot input sequence, the specific pilot input is indicated in the time series. The steps in the measured strain in response to the stepped inputs to the collective (SC) are clear in each data set. The responses to the collective doublet (CD) input are also clearly visible in figure 11, with top-hat changes of strain of amplitude approximately 150 $\mu\epsilon$ apparent in the data from both the FSI and and FBG sensors.
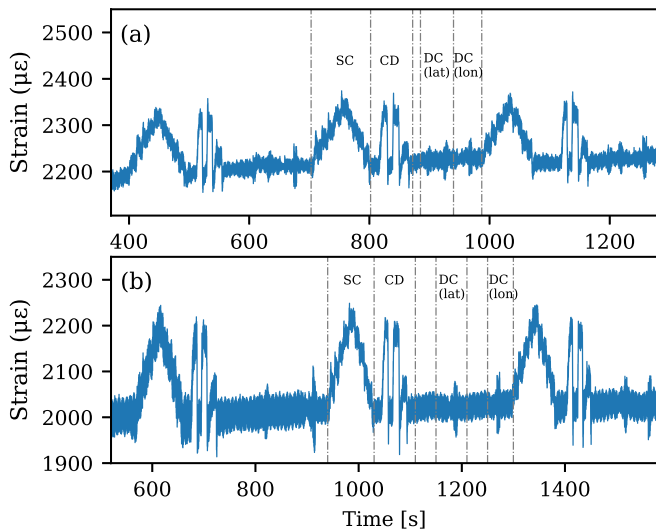
Figure 11. Strain data at full data rate, extracted from the time series shown in figure 8 for (a) FBG sensor G7 and (b) FSI sensor S7. The data include that recorder during the sequence of pilot collective and cyclic control inputs: SC—stepped collective, CD—collective doublet, DC (lat)—doublet cyclic lateral, DC (lon)—doublet cyclic longitudinal. For clarity, only the responses to the 2nd repeat of the sequence of inputs are labelled explicitly.
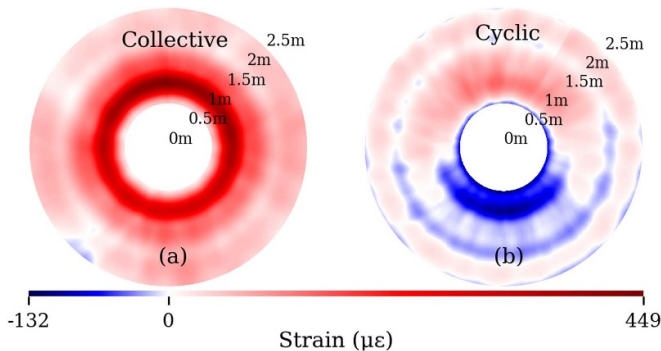

Figure 12. Changes in the strain distribution over a single rotation of the blade, relative to the average strain distribution during normal, 6.6 Hz rotation rate, operation. (a) Collective input and (b) cyclic input.

The responses to the cyclic inputs recorded can also be seen in figure 11. With reference to the inputs shown in figure 5, it can be concluded that the strains induced by movement of the cyclic control from neutral to left and back to neutral, and from neutral forward and back to neutral are clearly visible, but movement to the right and backwards are less apparent. As will be seen in section 4.3 the cyclic inputs induce a measurable dynamic behaviour to the blade.

The pilot input induced changes in the strain distribution along the blade over one rotation, relative the average distribution during normal, 6.6 Hz, rotation rate (plotted in figure 9), can be represented by a polar plot, as shown in figure 12 for the FSI data. This provides a clearer means for interpreting the responses shown in figure 8. The plots were generated by performing a cubic spline interpolation of the strains measured

by each fibre segment over a single time sample to generate the strain profile, from which the average strain distribution during normal operation was numerically subtracted. This was repeated over the time samples comprising a single rotation and a polar plot of the strain distribution was generated. Note that the choice of the reference azimuth is arbitrary. The response to the collective input indicates a largely rotationally symmetric strain change, as would be expected as the pitch of the blade is constant over the entire rotation. Radially, it can be seen that the effect of the change in pitch is to increase the loading, with the maximum change at the location where the pitch control cuff merges with the main structure of the blade, suggesting that the blade is bending further upwards than it does when there is no collective input. The fine structure in the plot is indicative of the excitation of vibration modes of the blade. During the cyclic excitation, where the blade changes pitch over the rotation cycle, the response is no longer rationally symmetric, with the location where the pitch control cuff merges with the main structure of the blade exhibiting a cyclical variation in loading relative to the average strain distribution for normal operation.

4.3. Frequency analysis

As is evident from the data presented, the time series contain rich information on the dynamics of the rotor blade. The spectra of the strain data time series were computed using Welch's method [36] over 50 s long sections of the time series, to estimate the power spectral density and then, by taking the square root of the spectra, to yield the strain amplitude spectral density. Figures 13(a) and (b) show the frequency spectra of the data from the FBG and the FSI segment, respectively, under two conditions: during the sections of the two ground runs at full rotation rate (avoiding sections containing pilot inputs to the controls) (black trace) presented in figure 11, and with the rotor stationary, but with the engine powered up (grey trace).

In the data captured at full rotation rate, the 1/rev rotor frequency and its harmonics (indicated by the dotted vertical lines) are present, as are a number of discrete frequencies that correspond to the aeroelastic flapping, torsion and lagging modes. The identification of the natural frequencies of a non-rotating BMR rotor blade via analysis of data recorded by FBG and DFOSS sensors during ground vibration tests undertaken in a laboratory was reported in [18, 19]. In the case of the data reported here, recorded with the blade rotating, the blade's stiffness changes resulting from the centrifugal forces and aeroelastic loading would be expected to alter the blade vibration frequencies [37]. Thus the sources of the observed frequency components are not discussed here, but their identification is the subject of on-going work.

The difference between the noise floors of the two instruments is clear in the data obtained with the rotor stationary, represented by the grey traces in figure 13. The excitation of natural modes of the stationary blade by environmental perturbations and by the vibrations from the engine (all the way up to modes at ≈50 Hz) can be clearly observed in the FSI data whereas above 4 Hz these vibration amplitudes are below
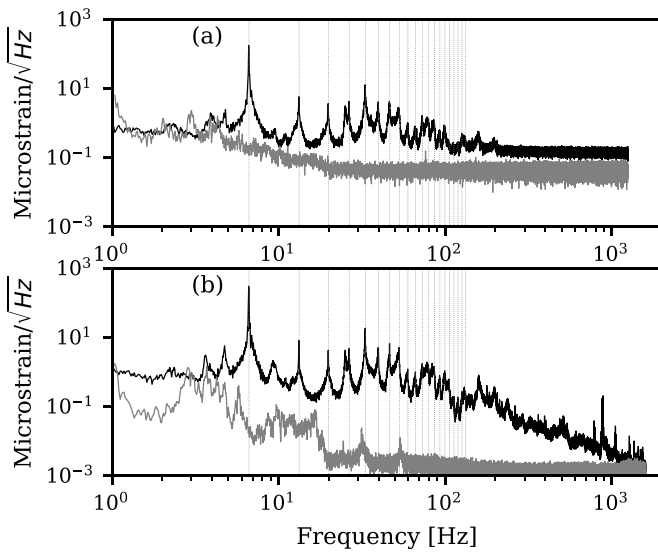
Figure 13. Strain amplitude spectral density of the strain signal determined using Welch's method (a) FBG sensor G7 and (b) FSI sensor S7. In each plot, the black trace represents the data acquired at full 6.6 Hz rotation speed, while the grey trace represents the data acquired when the rotor was not rotating, but with the helicopter engine powered up. The dotted lines indicate the first 20 1/rev rotor frequency harmonics.

Figure 14. Strain amplitude spectral density of the strain signal from FSI sensor S7 determined using Welch's method at full rotor speed. (a), (d) Normal full rotation rate operation (6.6 Hz) with no pilot inputs. (b) Shows the spectral density of the signal during the collective input while (c) shows the modulus of the numerical difference between the spectra in (a) and (b). (e) Shows the spectral density of the signal during the cyclic input while (f) shows the modulus of the numerical difference between the spectra in (d) and (e).

the noise floor of the FBG system. The typical noise standard deviation of FSI data is 0.04 $\mu\varepsilon$ over an interferometric bandwidth of 33 kHz (decimated to 3.2 kHz data rate), approximately corresponding to 0.2 n$\epsilon/\sqrt{Hz}$, in line with previous results [29]. Because decimated data is used for the computation of figure 13(b), high frequency noise will be aliased into the baseband and consequently the noise floor that can be observed in figure 13(b) of 1 n$\epsilon/\sqrt{Hz}$ is higher by approximately a factor of the square root of the ratio of the bandwidths, i.e. $\sqrt{33/1.6} \approx 4.5$, and remains consistent with the value of 0.2 n$\epsilon/\sqrt{Hz}$ over the full 33 kHz bandwidth stated above.

For FBG strain data, typical noise standard deviations of 1.5 $\mu\varepsilon$ over the 2.5 kHz bandwidth were obtained, corresponding approximately to 30 n$\epsilon/\sqrt{Hz}$. This shows that, in this implementation, FSI has a sensitivity more than two orders of magnitude larger than that of the FBG interrogation system used here. This can be explained partially by the integration of the strain signal over the longer gauge length of the FSI sensor, but it also due to the inherently higher strain sensitivity of FSI even for comparable gauge lengths, a result also recently confirmed for fibre optic pressure sensing applications [38]. It is also worth noting that the FSI measurement principle delivers the exact integral of the strain data [27] and is therefore not negatively affected by strain gradients across the gauge length.

This difference in performance is also clear in the data recorded at full rotation rate, where, above a frequency of approximately 200 Hz, figure 13(a) shows that for the data recorded by the FBG sensor the modal excitation is lower than the instrumental noise floor. Meanwhile, figure 13(b) shows that, for the data from the FSI sensor, higher order vibration modes can be resolved all the way down to the Nyquist frequency of 1.6 kHz.
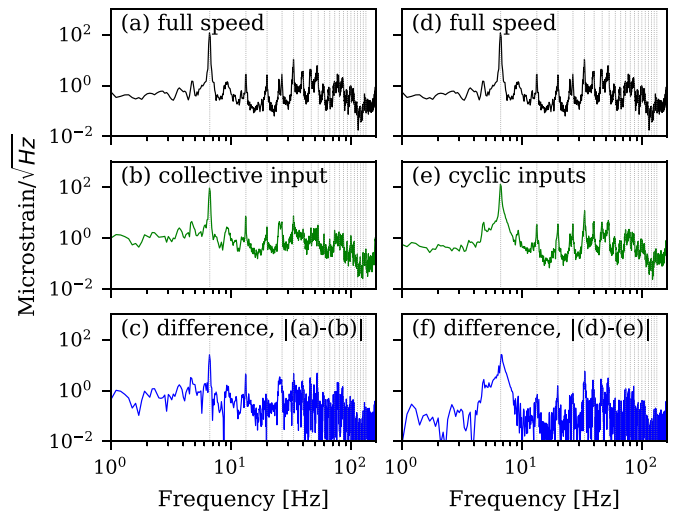
It is informative to plot the changes in the frequency spectra induced by the pilot inputs to the collective and cyclic controls. Here, the data from FSI sensor S7 are analysed. Figure 14 shows the frequency spectra of the measurements recorded under full speed, normal operation ((a) and (d)), compared with those obtained during the collective and cyclic pilot inputs, (b) and (e) respectively. The pilot-input-induced changes to the full-speed spectrum are shown in figures 14(c) and (f), for the collective and cyclic inputs, respectively.

Under all three flight conditions, it is believed that the 1st and 2nd lagging frequencies are observable at around 4.8 and 25 Hz. The redistribution of energy within the spectrum revealed by figure 14(c) provides evidence of the excitation of flapping structural modal frequencies, at 36.5 Hz (3rd flapping mode), 50 Hz (4th flapping mode) and 78 Hz (6th flapping mode), during the pilot inputs. In particular, the stepped collective input (figures 14(b) and (c)) are observed to have excited the first flapping mode, which is close to the first rotor harmonic. Due to the high aerodynamic damping, it was expected that the excitation of this mode would be difficult. During the cyclic control inputs (figures 14(e) and (f)), in addition to changes in the spectra at the frequencies noted above, there is a significant broadening of the peak at the fundamental 1/rev frequency. It should be noted that the ability to observe the aeroelastic modes in the frequency spectrum is highly sensitive to the location of the sensor element relative to the neutral axes of the underlying structure, which was discussed in a previous publication [18, 19].

To observe the operational vibration modes induced by each class of pilot input to the controls, the dynamics can be visualised using the spectrograms shown in figures 15(b)
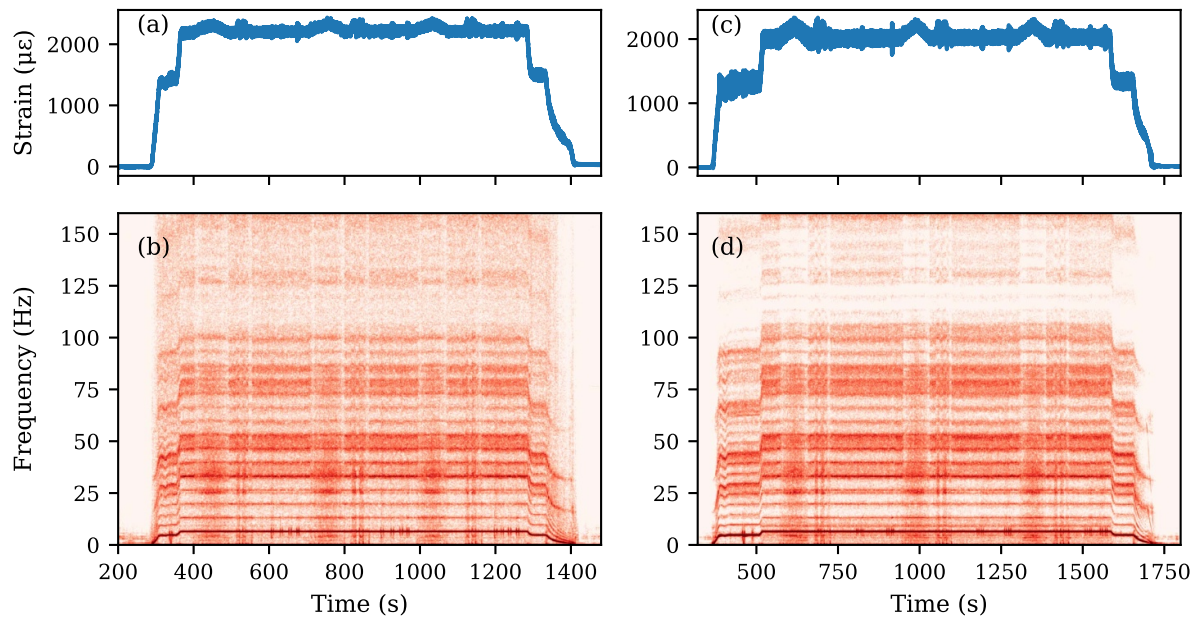
Figure 15. (a) and (d) Time series of the strain measured by fibre segment FBG G7 during ground run GR3. (b) Corresponding spectrogram. (c) Time series of the strain measured by FSI sensor S7 during ground run GR3, (d) corresponding spectrogram. Spectrograms determined by use of a short-time Fourier transform of the data time series.

and (d) for the FBG and FSI data, respectively, determined by taking the logarithm of the short-time Fourier transform of the time series (figures 15(a) and (b)), to localise the frequency components excited in time. The rotor harmonics are visible as the sharp lines in the plot. The blade vibration modes are broader and show a small dependence on the helicopter rotation speed. The frequencies of these natural modes increase with higher rotor frequency due to the subsequently larger blade stiffness that is a result of the additional centrifugal forces and aeroelastic loading. The excitation of the natural modes of the blade by the pilot inputs is revealed by observation of the changes in the distribution of energy in the spectrum, for example during the stepped collective pilot input sequence centred at approximately 650 s in the FSI data series in figure 15(b). Here the peak at 4.8 Hz can be seen to be more apparent and the broadening around the 4th, 5th and 6th harmonics of the rotation frequency can be seen, matching the observations in figure 14. During the the cyclic inputs, centred at 850 s in figure 15(b), the local broadening of the peaks at the rotation frequency, along with the blade's 1st flapping mode's vibration frequency, apparent in figure 14(e), are visible as the sharp vertical features. It is interesting to note that the responses to all of the pilot inputs to the cyclic controls are clearly visible in the spectral response in figures 15(b) and (d) (the two sets of four vertical features centred around the 1/rev rotation frequency, for example between 800 and 950 s in figure 15(b), corresponding the movements neutral—right, right—neutral, neutral—left and left—neutral, and from neutral—forward etc), while in the time series the movements to the right and backwards were obscured by the 1/rev signal.

The dependence of the blade's natural vibration frequencies on the helicopter rotation rate is apparent in figures 15(b) and (d), in the regions of the spectrograms corresponding to the

reduction in rotor speed (>1350 and >1650 s, respectively). Here the sharper lines corresponding to the rotor harmonics fall rapidly to 0 Hz, while the diffuse lines characteristic of the blade's natural frequencies fall to their values measured when the blade is not loaded. Observing the modes in this way may allow the generation of the complete Campbell diagram of the helicopter blade, which presents the blade's response spectrum in terms of the rotation oscillation rate, providing useful information for blade characterisation and health monitoring, with changes being indicative of damage [39]. The use of highly localized strain measurements and of methods based on curvature mode shape was reported to be very effective for damage localisation [40], which is the subject of further studies.

5. Conclusions

The deployment of two optical fibre-based strain sensing approaches, FBG and FSI, on the main rotor blades of a helicopter during a series of full rotational speed ground runs has been described. It has been shown that the fibre optic sensors were capable of providing measurements of the strain experienced by the blades and of the characterisation of the blade dynamics, excited by specific pilot inputs to the collective and cyclic controls. Both sensing approaches were capable of detecting the 1/rev rotation frequency, and its harmonics, and of detecting the operational aeroelastic modes excited by specific pilot inputs. The FSI system was demonstrated to have a two orders of magnitude lower noise floor than that exhibited by the FBG system, with strain noise standard deviations of 0.2 $n\epsilon/\sqrt{Hz}$ for the FSI and 30 $n\epsilon/\sqrt{Hz}$ for the FBG-based sensing approach. The superior performance of the FSI system

be explained partially by the longer gauge length of the FSI sensor, and it also demonstrates the inherently higher strain sensitivity of FSI.

In general, for applications such as the evaluation of blade dynamics, it can be concluded that highly localized strain sensing provided by the FBG system is not required, and that the averaging of strain over longer gauge lengths is beneficial due to the increase in sensitivity, due to the improvement in signal to noise ratio. In addition, long-gauge length sensing makes the measurement less sensitive to local structural inhomogeneities or local non-idealities in strain transfer. Both systems have been demonstrated to be sufficiently rugged for deployment in the hostile environment of a rotating helicopter hub, providing powerful tools for the validation of blade designs and for in-service blade condition monitoring. Relating the data to the aeroelastic properties of the blade will be the subject of future publications.

Data availability statement

The data that support the findings of this study are openly available at the following URL/DOI: 10.17862/cranfield. rd.16974649.

Acknowledgments

ORCID iDs

Stephen W James https://orcid.org/0000-0003-0651-9842
Thomas Kissinger https://orcid.org/0000-0003-1832-7143
Thomas O H Charrett https://orcid.org/0000-0002-6677-7264
Ralph P Tatam https://orcid.org/0000-0001-9599-3639

References

[1] Cusano A, Cutolo A and Albert J 2018 *Fiber Bragg Grating Sensors: Recent Advancements, Industrial Applications and Market Exploitation* (Bentham Science Publishers)

[2] Lawson N J, Correia R, James S W, Partridge M, Staines S E, Gautrey J E, Garry K P, Holt J C and Tatam R P 2016 Development and application of optical fibre strain and pressure sensors for in-flight measurements *Meas. Sci. Technol.* **27** 104001

[3] Read I J and Foote P D 2001 Sea and flight trials of optical fibre bragg grating strain sensing systems *Smart Mater. Struct.* **10** 1085–94

[4] Chehura E, James S W, Staines S, Groenendijk C, Cartie D, Portet S, Hugon M and Tatam R P 2020 Production process monitoring and post-production strain measurement on a full-size carbon-fibre composite aircraft tail cone assembly using embedded optical fibre sensors *Meas. Sci. Technol.* **31** 105204

[5] Serafini J, Bernardini G, Porcelli R and Masarati P 2019 In-flight health monitoring of helicopter blades via differential analysis *Aerosp. Sci. Technol.* **88** 436–43

[6] Dragan K 2011 Structural health monitoring and damage detection of the helicopter main rotor blades with the structure integrated sensors *7th DSTO Int. Conf. on Health & Usage Monitoring, AIAC14 14th Australian Int. Aerospace Congress*

[7] Ramirez A S, Loendersloot R, Jauregui J M and Tinga T 2013 Design framework for vibration monitoring systems for helicopter rotor blade monitoring using wireless sensor networks *Structural Health Monitoring 2013* ed F K Chang pp 1039–46

[8] Wells D A, Frattini T, Chruchill D L and DiStasi S 2014 Development of a helicopter on-rotor hum system powered by energy harvesting *40th European Rotorcraft Forum 2014*

[9] Golub R and McLachlan W 1967 In-flight measurement of rotor blade airloads, bending moments, and motions, together with rotor shaft loads and fuselage vibration, on a tandem rotor helicopter *Technical Report 67-9A* (U.S. Army Aviation Materiel Laboratories)

[10] Grant W J and Pruyn R R 1967 In-flight measurement of rotor blade airloads,bending moments, and motions, together with rotor shaft loads and fuselage vibration, on a tandem rotor helicopter *Technical Report 67-9B* (U.S. Army Aviation Material Laboratories)

[11] Riley J, Padfield G D and Smith J 1988 Estimation of rotor blade incidence and blade deformation from the measurement of pressures and strains in flight *14th European Rotorcraft Forum (Milan, Italy)* pp 1–20

[12] Sirohi J and Lawson M S 2012 Measurement of helicopter rotor blade deformation using digital image correlation *Opt. Eng., Bellingham* **51** 4

[13] Betz D, Staudigel L, Trutzel M N, Schmuecker M, Huelsmann E and Czemay U 2002 Test of a fiber bragg grating sensor network for commercial aircraft structures *15th Optical Fiber Sensors Conf. Technical Digest, OFS 2002* pp 55–58

[14] Lawson N J, Correia R, James S W, Gautrey J E, Rubio G I, Staines S E, Partridge M and Tatam R P 2017 Development of the cranfield university bulldog flight test facility *Aeronaut. J.* **121** 533–52

[15] Wada D, Igawa H, Tamayama M, Kasai T, Arizono H and Murayama H 2019 Flight demonstration of aircraft wing monitoring using optical fiber distributed sensing system *Smart Mater. Struct.* **28** 055007

[16] Kim J-H, Park Y, Kim Y-Y, Shrestha P and Kim C-G 2015 Aircraft health and usage monitoring system for in-flight strain measurement of a wing structure *Smart Mater. Struct.* **24** 105003

[17] Kim J-H, Shrestha P, Park Y and Kim C-G 2014 Application of fiber bragg grating sensors in light aircraft: ground and flight test *Proc. SPIE* **9157** 91578V

[18] Kissinger T, Weber S, Chehura E, Barrington J, Staines S, James S W, Lone M and Tatam R P 2019 Ground vibration testing of a helicopter rotor blade using optical fibre sensors *Proc. SPIE* **11199** 1119902

[19] Weber S *et al* 2021 Application of fibre optic sensing systems to measure rotor blade structural dynamics *Mech. Syst. Signal Process.* **158** 107758

[20] Kim S B, Geiger D, Bowles P O, Matalanis C G and Wake B E 2016 Tip displacement estimation using fiber optic sensors for x2 technology rotor blades *AHS Int. 72nd Annual Forum* pp 1914–23

[21] Hajek M, Manner S and Susse S 2015 Blade root integrated optical fiber Bragg grating sensors a highly redundant data source for future HUMS *AHS Int. 71st Annual Forum (Virginia Beach, Virginia, USA)* pp 1598–605

[22] Serafini J, Bernardini G, Mattioni L, Vezzari V and Ficuciello C 2017 Non-invasive dynamic measurement of helicopter blades *J. Phys.: Conf. Ser.* **882** 012014

[23] Weber S *et al* 2018 Bladesense—a novel approach for measuring dynamic helicopter rotor blade deformation *44th European Rotorcraft Forum*

[24] Kissinger T *et al* 2022 Fibre-optic measurement of strain and shape on a helicopter rotor blade during a ground run: 2. Measurement of shape *Smart Mater. Struct.* accepted (https://doi.org/10.1088/1361-665X/ac736c)

[25] Kashyap R 2009 *Fiber Bragg Gratings* 2nd Edition (Burlington: Academic Press)

[26] Smart Fibers Ltd 2020 SmartScan Aero Mini User Manual (available at: www.smartfibres.com/products/smartscan-aero-mini) (Accessed 1 June 2022)

[27] Kissinger T, Correia R, Charrett T O H, James S W and Tatam R P 2016 Fiber segment interferometry for dynamic strain measurements *J. Lightwave Technol.* **34** 4620–6

[28] Kissinger T, Charrett T O H and Tatam R P 2015 Range-resolved interferometric signal processing using sinusoidal optical frequency modulation *Opt. Express* **23** 9415–31

[29] Kissinger T, Chehura E, Staines S E, James S W and Tatam R P 2018 Dynamic fiber-optic shape sensing using fiber segment interferometry *J. Lightwave Technol.* **36** 917–25

[30] James S W, Kissinger T, Weber S, Mullaney K, Chehura E, Barrington J H and Tatam R 2022 Fibre-optic measurement of strain and shape on a helicopter rotor blade during a ground run: data for the measurement of strain *Cranfield Online Data Repository* (https://doi.org/10.17862/cranfield.rd.16974649)

[31] Bertholds A and Dandliker R 1988 Determination of the individual strain-optic coefficients in single-mode optical fibres *J. Lightwave Technol.* **6** 17–20

[32] Kissinger T, Charrett T O H and Tatam R P 2013 Fibre segment interferometry using code-division multiplexed optical signal processing for strain sensing applications *Meas. Sci. Technol.* **24** 094011

[33] Roths J and Jülich F 2008 Determination of strain sensitivity of free fiber Bragg gratings *Proc. SPIE* **7003** 73–80

[34] Bansemir H and Emmerling S 1999 Fatigue substantiation and damage tolerance evaluation of fiber composite helicopter components *RTO AVT Specialists' Meeting on Application of Damage Tolerance Principles for Improved Airworthiness of Rotorcraft (Corfu, Greece, 21–22 April 1999)*

[35] Kinet D, Mégret P, Goossen K W, Qiu L, Heider D and Caucheteur C 2014 Fiber bragg grating sensors toward structural health monitoring in composite materials: challenges and solutions *Sensors* **14** 7394–419

[36] Welch P 1967 The use of fast fourier transform for the estimation of power spectra: a method based on time averaging over short, modified periodograms *IEEE Trans. Audio Electroacoust.* **15** 70–73

[37] Rammer R, Priems M and Konstanzer P 2013 Modification of a four bladed main rotor—impact on dynamics and vibrations *39th European Rotorcraft Forum (Moscow, Russia, 3–6 September 2013)* pp 1–10

[38] Aime L F J, Kissinger T, James S W, Chehura E, Verzeletti A and Tatam R P 2021 High sensitivity pressure measurement using optical fibre sensors mounted on a composite diaphragm *Opt. Express* **29** 4105–23

[39] Badshah S, Naeem A, Farhan R A, Ul Haq I and Abdullah Malik S 2019 Numerical study on the critical frequency response of jet engine rotors for blade-off conditions against bird strike *Appl. Sci.* **9** 5568

[40] Fan W and Qiao P 2011 Vibration-based damage identification methods: a review and comparative study *Struct. Health Monit.* **10** 83–111